



# Ultrathin porous carbon nitride nanosheets with well-tuned band structures via carbon vacancies and oxygen doping for significantly boosting H<sub>2</sub> production



Bin Yang <sup>a,1</sup>, Xiaolong Li <sup>a,1</sup>, Qian Zhang <sup>a</sup>, Xiaodong Yang <sup>a</sup>, Jianguo Wan <sup>a</sup>, Guangfu Liao <sup>b,\*</sup>, Jiaojiao Zhao <sup>a</sup>, Rongjie Wang <sup>a</sup>, Jichang Liu <sup>a</sup>, Raul D. Rodriguez <sup>c,\*</sup>, Xin Jia <sup>a,\*</sup>

<sup>a</sup> School of Chemistry and Chemical Engineering/Key Laboratory for Green Processing of Chemical Engineering of Xinjiang Bingtuan, Key Laboratory of Materials-Oriented Chemical Engineering of Xinjiang Uygur Autonomous Region, Engineering Research Center of Materials-Oriented Chemical Engineering of Xinjiang Bingtuan, Shihezi University, Shihezi 832003, China

<sup>b</sup> Engineering Research Center of Nano-Geomaterials of Ministry of Education, China University of Geosciences, Wuhan 430074, China

<sup>c</sup> Tomsk Polytechnic University, 30 Lenin Avenue, 634050 Tomsk, Russia

## ARTICLE INFO

### Keywords:

Photocatalysis

g-C<sub>3</sub>N<sub>4</sub>

Carbon vacancies

Oxygen doping

H<sub>2</sub> generation

## ABSTRACT

Significant improving g-C<sub>3</sub>N<sub>4</sub>'s photocatalytic efficiency still remains a great challenge. In this work, we synthesized ultrathin and porous 2D g-C<sub>3</sub>N<sub>4</sub> nanosheets with a controllable concentration of carbon vacancies and oxygen doping. Water vapor opens the heptazine units, introduces carbon vacancies, and acts as an oxygen source for oxygen doping under high temperatures. The synergistic effect of controllable carbon vacancies and oxygen doping can continuously regulate band structures and significantly improves the separation efficiency of photoexcited charges. As a result, the prepared g-C<sub>3</sub>N<sub>4</sub> with vigorous reduction potential exhibits a very high photocatalytic H<sub>2</sub> evolution rate of 2.414 mmol g<sup>-1</sup> h<sup>-1</sup> under visible light and 7.414 mmol g<sup>-1</sup> h<sup>-1</sup> under ultraviolet-visible light, respectively, which outperforms the majority of the previously reported g-C<sub>3</sub>N<sub>4</sub> with well-tuned band structure. This work offers a new design idea for highly active g-C<sub>3</sub>N<sub>4</sub>-based photocatalysts with a well-tuned band structure.

## 1. Introduction

The Water splitting to carbon-free green hydrogen (H<sub>2</sub>) using inexhaustible solar energy via artificial photosynthesis is considered one of the most attractive topics in catalysis, materials science, and energy [1]. Superior photocatalysts with appropriate energy band structure, green, low cost, and stable physicochemical properties are crucial for industrialization and large-scale development of photocatalysis to produce H<sub>2</sub> and satisfy our energy needs in the future [2]. Graphitic carbon nitride (g-C<sub>3</sub>N<sub>4</sub>) polymers with stable structure, easy preparation, and non-toxic characteristics have been widely studied to achieve photocatalytic hydrogen evolution reaction (HER) [3]. However, the pristine g-C<sub>3</sub>N<sub>4</sub> comprises heavily thick aggregates with a nasty combination of photoexcited charges and a limited number of exposed active sites on the surface, which severely restrict photocatalytic HER activity [4]. In addition, the intrinsic electronic structure and low-grade reduction

potential of g-C<sub>3</sub>N<sub>4</sub> result in low photocatalytic activity [5]. Therefore, engineering g-C<sub>3</sub>N<sub>4</sub> to achieve strong reduction potential, high carrier utilization efficiency, and highly exposed active sites remain a critical challenge.

In contrast to thick flakes, 2D ultrathin g-C<sub>3</sub>N<sub>4</sub> nanosheets demonstrated remarkable application potential in photocatalysis due to tunable vacancies/doping on its surface, adjustable band structure, highly exposed active sites, and high carrier utilization efficiency [6,7]. Various physical and chemical stripping strategies are being developed to obtain ultrathin and porous g-C<sub>3</sub>N<sub>4</sub> nanosheets, including strong acid exfoliation [8], ultrasonic exfoliation [9], and thermal exfoliation in different atmospheres [10], etc. [11]. However, those nanosheets previously reported have many limitations due to their strong intralayer chemical bonding and interlayer interactions (including van der Waals interaction and hydrogen bonds). In other words, following the single-step stripping methods makes it challenging to obtain uniform,

\* Corresponding authors.

E-mail addresses: [liaogf@mail2.sysu.edu.cn](mailto:liaogf@mail2.sysu.edu.cn) (G. Liao), [raul@tpu.ru](mailto:raul@tpu.ru) (R.D. Rodriguez), [jiaxin@shzu.edu.cn](mailto:jiaxin@shzu.edu.cn) (X. Jia).

<sup>1</sup> These authors contributed equally to this work.

high-quality, and ultrathin nanosheets and synchronously create porous structures on the photocatalyst surface [12]. The step-by-step synergistic etching/stripping can fully play the advantages of each stripping step, which can efficiently exfoliate g-C<sub>3</sub>N<sub>4</sub> with high-quality, uniform, and ultrathin porous nanosheets [13].

In addition, the oxygen doping into g-C<sub>3</sub>N<sub>4</sub> has also attracted extensive attention because it can evidently change the material's band structure [14] and simultaneously accelerate the separation of photo-excited charges [15,16]. Besides, the vacancies also play a crucial role in promoting photocatalytic HER [17], which usually are introduced into the heptazine framework in the stripping process of g-C<sub>3</sub>N<sub>4</sub> opening a path to regulate band structure [18,19] and serve as charges trapping center to promote spatial separation of photoexcited charges [20]. For instance, Yang et al. reported a general etching protocol to construct nitrogen vacancies on the surface of g-C<sub>3</sub>N<sub>4</sub> [21], but this method is not environmentally friendly. Wang et al. reported carbon-deficient g-C<sub>3</sub>N<sub>4</sub> by steam reforming strategy [22,23]. However, the inadequate stripping results in a small specific surface area with limited exposure to active sites. Water is the greenest and cheapest solvent. It is believed that water vapor can introduce carbon vacancies undergoing reforming reaction [24] and act as a source of oxygen to achieve oxygen doping undergoing hydrolysis reaction [25] under high temperature. Therefore, a green step-by-step synergistic etching/stripping method is worthy of consideration for preparing ultrathin and porous g-C<sub>3</sub>N<sub>4</sub> nanosheets with controllable carbon vacancies and oxygen doping, which can integrate the advantages mentioned above and synergistically improve photocatalytic activity.

Inspired by these expected benefits, we implemented the above strategy to obtain ultrathin and porous 2D g-C<sub>3</sub>N<sub>4</sub> nanosheets (TCN-460) with controllable carbon vacancies and oxygen doping. This was possible with a step-by-step synergistic etching/stripping strategy, where the pristine g-C<sub>3</sub>N<sub>4</sub> [26] undergoes thermal etching/stripping in air combined with subsequent water vapor assisted thermal etching/stripping. Elemental analysis, positron annihilation spectra, electron paramagnetic resonance spectroscopy, C K-edge XANES spectra, and X-ray photoelectron spectroscopy (XPS) results show that the surface of TCN-460 has carbon vacancies with controllable concentration by the water vapor reforming reaction of g-C<sub>3</sub>N<sub>4</sub> under high temperature. Furthermore, the fitted O 1 s and C 1 s XPS spectra showed that water vapor also acts as an oxygen source to introduce controllable oxygen doping by the hydrolysis reaction. Because of the high sensitivity of electronic structure to the microenvironment on the semiconductor surface, the bandgap widens, and the valence and conduction bands move up when carbon vacancies and oxygen doping are introduced into ultrathin porous g-C<sub>3</sub>N<sub>4</sub> nanosheets, which provide a strong driving force for photocatalytic HER. The synergistic effect of controllable carbon vacancies and oxygen doping in ultrathin and porous g-C<sub>3</sub>N<sub>4</sub> nanosheets significantly improves the separation and migration of photoexcited charges. As expected, the prepared TCN-460 demonstrates excellent photocatalytic HER as high as 2.414 mmol g<sup>-1</sup> h<sup>-1</sup> under visible light irradiation ( $\lambda \geq 420$  nm), 14.42 times better than pristine g-C<sub>3</sub>N<sub>4</sub>. Due to its wide bandgap and strong reduction ability, TCN-460 also exhibits 7.414 mmol g<sup>-1</sup> h<sup>-1</sup> photocatalytic HER activity under ultraviolet-visible light (780 nm  $\geq \lambda \geq 350$  nm), which is 5.2 times higher than pristine g-C<sub>3</sub>N<sub>4</sub>.

## 2. Experimental section

### 2.1. Preparation of PCN

PCN was prepared according to the literature procedure [27]. 5 g of melamine was calcined at 550 °C for 4 h in a muffle furnace at 5 °C/min. The obtained yellow powder was denoted as PCN.

### 2.2. Preparation of TCN

The covered corundum crucible containing 0.5 g of PCN was calcined at 520 °C for 4.5 h at 5 °C/min in a muffle furnace under a controlled air atmosphere. The obtained light yellow powder was denoted as TCN.

### 2.3. Preparation of TCN-400, TCN-430 and TCN-460

See Fig. 1a; the corundum crucible containing 0.5 g of TCN was calcined at a specified temperature (400 °C, 430 °C, and 460 °C) for 1 h at 5 °C/min in a tube furnace. During the heating process, the water vapor, heated to 130 °C, is carried into the tube furnace through argon (Ar) gas at a 40 mL/min flow rate. The powders were denoted as TCN-400, TCN-430, and TCN-460 according to different calcination temperatures.

### 2.4. Preparation of PCN-460 and TCN-Ar

The preparation of PCN-460 is similar to TCN-460, except that TCN is replaced with PCN. The preparation of TCN-Ar is the same as that of TCN-460, except for the absence of water vapor.

### 2.5. Photoelectrochemical measurement

The electrochemical measurements were recorded on a CHI 760D electrochemical workstation with a standard three-electrode system under visible and ultraviolet-visible light irradiation (PLS-SXE 300 C (BF); PerfectLight, Beijing). The saturated Ag/AgCl electrode, Pt foil, and fabricated photoanode were used as reference electrode, counter electrode, and working electrode, respectively.

### 2.6. Photocatalytic reaction and quantum yield measurements

The photocatalytic HER was acquired on an on-line analytical system (Labsolar-III, PerfectLight, Beijing). The optimal mass of catalyst (20 mg) was dispersed in 100 mL of 10 vol% triethanolamine (TEOA) aqueous solution, 3 wt% Pt was in-situ photodeposited on the surface of photocatalysts by adding H<sub>2</sub>PtCl<sub>6</sub>. A 300 W Xenon lamp with/without a UV-cutoff filter ( $\lambda > 420$  nm) was used as the light source. Before photocatalytic HER began, the reaction cell was evacuated for 1 h to remove the air altogether. The amount of H<sub>2</sub> gas produced was detected by gas chromatography. The apparent quantum yield (AQY) was measured under various monochromatic lights (365 nm, 420 nm, 500 nm, and 550 nm), and the AQY was calculated according to the following Equation [6]:

$$\begin{aligned} \text{AQY}(\%) &= \frac{\text{number of reacted electrons}}{\text{number of incident photons}} \times 100\% \\ &= \frac{\text{number of hydrogen molecules} \times 2}{\text{number of incident photons}} \times 100\% \end{aligned}$$

### 2.7. Computation

DFT calculations were performed within the General Gradient Approximate (GGA) functional using the plane-wave-based Vienna Ab-initio Simulation Package (VASP) code. The vacuum space was set to 20 Å, which has been proven large enough to avoid the layer-to-layer effects. The cutoff energies for plane waves were 500 eV. A 6 × 6 × 1 Monkhorst-Pack k-point mesh was used in the geometry optimization and geometries of the composites were optimized separately until the force on each atom was less than 10<sup>-4</sup> eV Å<sup>-1</sup>.

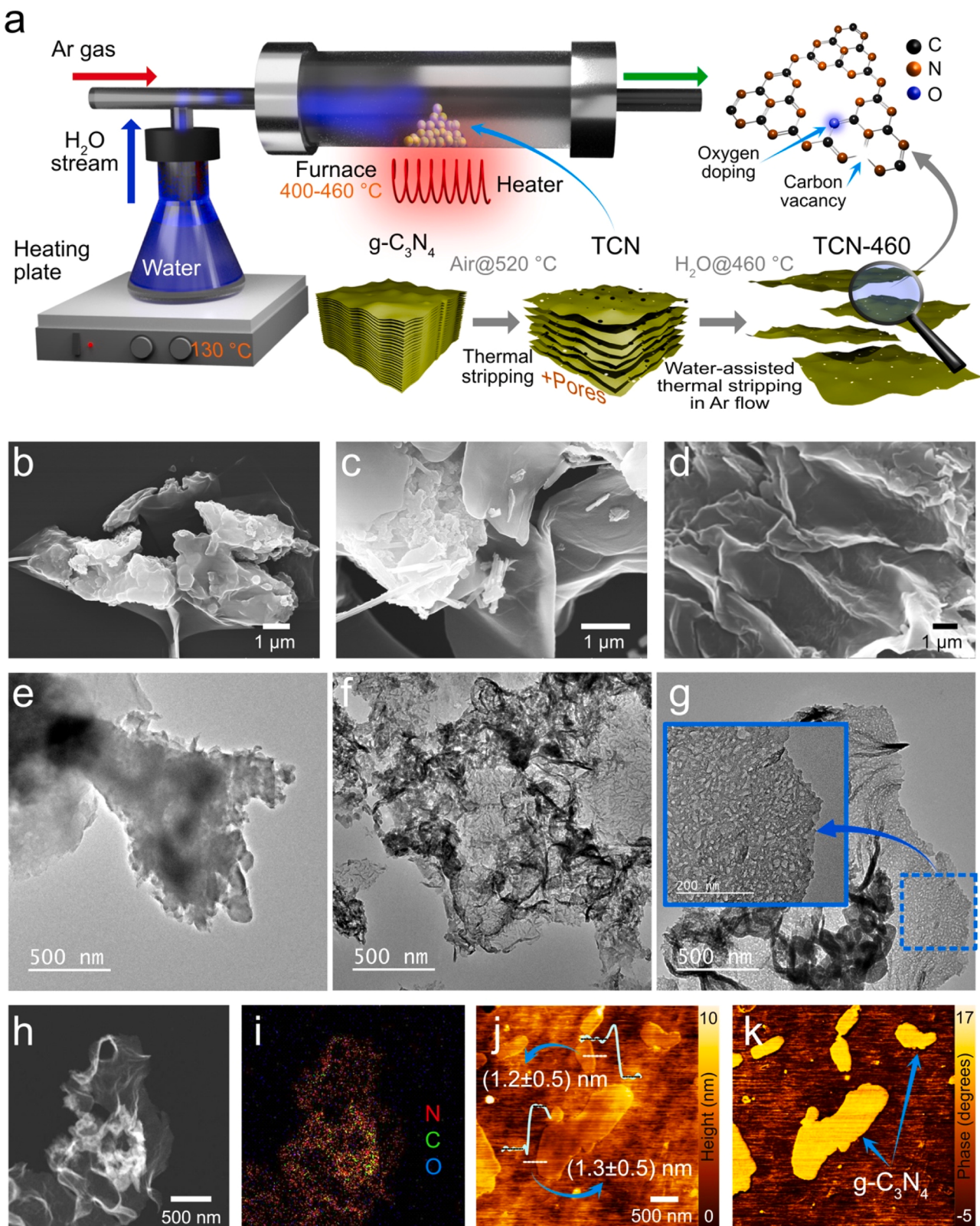


**Fig. 1.** (a) Schematic illustration of the synthesis route of TCN-460; (b, c, d) SEM and (e, f, g) TEM of PCN, TCN, and TCN-460; (h, i) C, N, O elemental mapping of TCN-460; (j, k) AFM phase imaging corresponding height profiles and topography of TCN-460.

### 3. Results and discussion

#### 3.1. Synthesis of ultrathin $\text{g-C}_3\text{N}_4$ nanosheets with high porosity

We prepared ultrathin and porous  $\text{g-C}_3\text{N}_4$  nanosheets with controllable carbon vacancies and oxygen doping by a step-by-step synergistic etching/stripping strategy (Fig. 1a). SEM images show that the step-by-step synergistic etching/stripping strategy gradually transforms the thick aggregates of  $\text{g-C}_3\text{N}_4$  into wrinkled and ultrathin nanosheets (Fig. 1b-d). TEM results in Fig. 1e-g confirmed this observation, showing the  $\text{g-C}_3\text{N}_4$  aggregates' gradual transformation into ultrathin and semi-transparent nanosheets with a high density of surface pores. The elemental mapping images in Fig. 1i evidence the uniform distribution of C, N, and O elements. AFM topography and phase imaging with the corresponding height profiles demonstrate that the TCN-460 exists as nanosheets with an average thickness of about 1.2 nm (Fig. 1j-k) [27]. The phase image in Fig. 1k clearly shows the chemical differences between the substrates and TCN-460 nanosheets. BET confirms the specific surface area increase from PCN and TCN to TCN-460, and the water vapor-assisted thermal etching/stripping has the most significant impact on the surface area. The pore size distribution results in Fig. 2b show that the surface of TCN-460 obtained by water vapor-assisted thermal etching/stripping contains a more significant number of mesopores and macropores than PCN and TCN. Because of the increase in specific surface area, TCN-460 has the most pronounced volume expansion (Fig. S1). These results indicate that ultrathin  $\text{g-C}_3\text{N}_4$  nanosheets with abundant pores and high specific surface area are successfully prepared by a step-by-step synergistic etching/stripping strategy.

XRD was used to characterize the crystal structure of samples. All

samples exhibit intense diffraction peaks around  $13.1^\circ$  and  $27.9^\circ$  indexed to (100) and (002) planes of hexagonal  $\text{g-C}_3\text{N}_4$  (JCPDS card no. 87-1526) [28]. These reflections correspond to the tri-s-triazine units and the interlamellar distance, respectively (Fig. 2d). Compared with PCN, the (002) diffraction peak intensity from TCN is weaker, mainly due to the partial stripping of stack aggregates of PCN by thermal/etching. TCN-400 has obviously stronger diffraction peaks intensity at  $27.9^\circ$  than that of TCN. This result shows that water vapor's thermal etch/stripping function can decrease the gallery distance between the basic sheets, leading to lifting crystallinity [7]. However, the two diffraction peaks become broader and weaker as the temperature of water vapor-assisted thermal etching/stripping increases, attributed to surface-structured defects in  $\text{g-C}_3\text{N}_4$  introduced by water vapor. This supports the  $\text{g-C}_3\text{N}_4$  nanosheets with surface disorder and in-plane ordered structure [29]. The FTIR spectra of all samples reveal the same  $\text{g-C}_3\text{N}_4$  chemical structure (Fig. 2e) [30,31]. Compared with PCN and TCN, the bending vibration peak intensities of amine groups decrease slightly when increasing the temperature of thermal etching/stripping by assisting water vapor. The result indicates that the  $\text{g-C}_3\text{N}_4$  surface structure is opened somewhat due to the function of water vapor.

#### 3.2. Characterization of carbon vacancies and oxygen doping in TCN-460

The organic element analysis is applied as an intuitive quantitative method to characterize the presence of carbon vacancies and oxygen doping [21]. The C/N elemental ratios of TCN and PCN are fairly close (Fig. 3a), indicating that thermal stripping etching in air introduced only a very small amount of vacancies. When TCN undergoes water

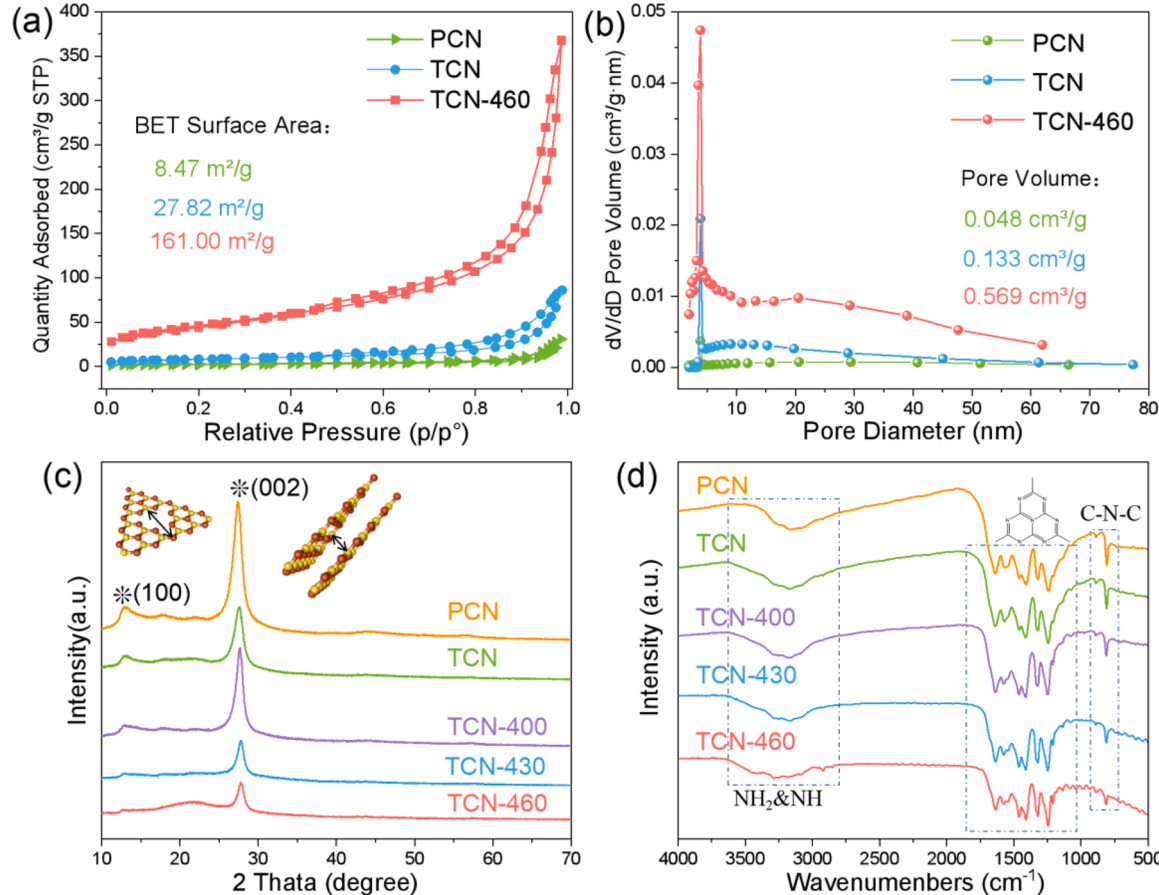
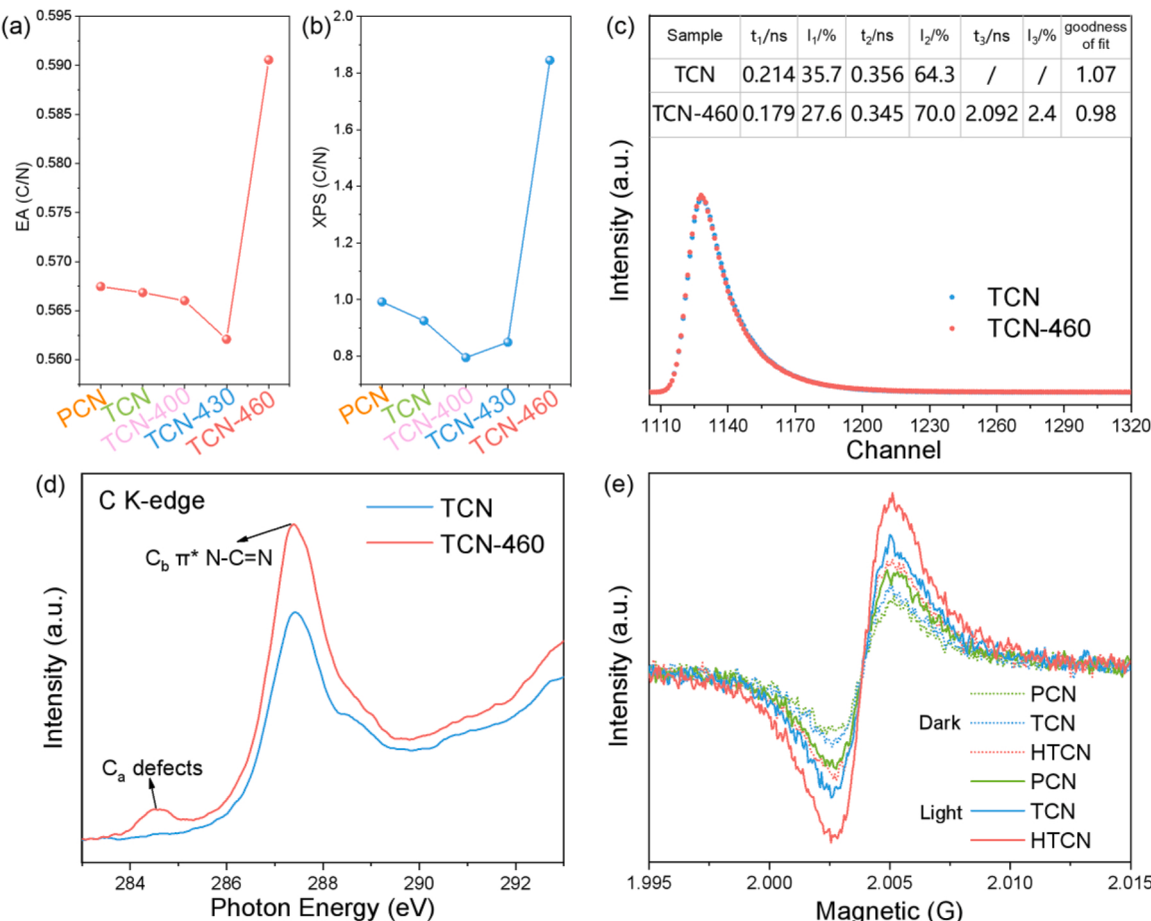


Fig. 2. (a)  $\text{N}_2$  adsorption-desorption isotherms, (b) the corresponding PSD curves of PCN, TCN, and TCN-460; (c) XRD spectra and (d) FTIR spectra of different samples: PCN, TCN, TCN-400, TCN-430, and TCN-460.



**Fig. 3.** The C/N atomic ratio of all samples obtained by organic element analysis (a) and XPS surface element analysis (b); (c) Positron annihilation spectra (PAS) and (d) C K-edge XANES spectra of TCN and TCN-460; (e) EPR spectra in dark or light of PCN, TCN, and TCN-460.

vapor-assisted thermal stripping/etching for temperatures below 430 °C, the C/N element ratio decreases with the increase of pyrolytic temperature. This indicates that the water vapor reforming reaction mainly occurs with the carbon atom at N-(C)<sub>3</sub> sites in g-C<sub>3</sub>N<sub>4</sub> [C<sub>n</sub>H<sub>m</sub> + n H<sub>2</sub>O → n CO + (n + m/2) H<sub>2</sub>] [22], resulting in the loss of carbon atoms and the formation of carbon vacancies. In contrast, when the pyrolytic temperature exceeds 430 °C, the C/N ratio increases significantly with the increase of pyrolytic temperature. We attribute this change as an indication of water vapor reacting selectively with nitrogen converting C-N=C groups into C-O-C accompanied by NH<sub>3</sub> release while inducing oxygen doping. The rate of introducing oxygen doping is much higher than the rate of forming carbon vacancies so that the C/N ratio is reversed. Indeed, using ion chromatography, 115 ppm of ammonium ions were detected in 3 mL of the collected aqueous solution from the reaction quartz tube, which comes from dissolved NH<sub>3</sub>. We also used XPS elemental analysis as a highly sensitive method to characterize C/N ratio changes caused by the introduction of carbon vacancies and oxygen doping (Fig. 3b) [32]. The variation trend of the C/N ratio with pyrolytic temperature is consistent with the results obtained from organic elemental analysis. Due to the surface-sensitive nature of XPS, the change of the C/N ratio is more evident from XPS results than results from organic elemental analysis. This difference indicates that the introduction of carbon vacancies and oxygen doping occurs at the surface of g-C<sub>3</sub>N<sub>4</sub>.

Positron annihilation spectra (PAS) are a powerful approach to comprehensively detecting and characterize carbon vacancies on the surface of g-C<sub>3</sub>N<sub>4</sub> [22]. The PAS lifetime (τ<sub>1</sub>) is attributed to small size vacancies, while the PAS lifetime (τ<sub>2</sub>) is related to large size vacancies in a material. It is generally accepted that small size vacancies exist in the

bulk of materials, while large ones lie on the surface. The PAS lifetime (τ<sub>3</sub>) is assigned to positron annihilation of orthopositronium atoms in the large voids in the materials. The lifetime intensity usually reflects the concentration of vacancies, as shown in the table inserted in Fig. 3c. Both TCN and TCN-460 exhibit τ<sub>1</sub> and τ<sub>2</sub>, indicating that both materials contain bulk and surface vacancies. The τ<sub>1</sub> intensity of TCN is remarkably larger than that of TCN-460, which suggests that the vacancies concentration in the interior of TCN is higher than that of TCN-460. However, internal vacancies act as recombination centers for photoexcited charges inhibiting the photocatalytic reaction performance. The τ<sub>2</sub> intensity of TCN-460 is significantly larger than TCN due to higher surface vacancy density in TCN-460 compared to TCN. The characteristics of TCN-460 with multiple external carbon vacancies and few internal ones significantly can improve the separation efficiency of photoexcited charges resulting in helpful photocatalytic HER activity. TCN-460 samples showed the presence of τ<sub>3</sub> but not TCN, indicating that water vapor etches the surface of g-C<sub>3</sub>N<sub>4</sub> and introduces large voids at high temperature, which is consistent with HRTEM and BET results.

Fig. 3d shows the C K-edge XANES spectra of PCN and TCN-460. There are two characteristic peaks at 284.5 eV (peak C<sub>a</sub>) and 287.4 eV (peak C<sub>b</sub>), corresponding to the structural vacancies and the π\* states (sp<sup>2</sup> hybridized N-C=N) of the C 2p orbital, respectively [31]. Compared with TCN, TCN-460 shows a clear C<sub>a</sub> peak, indicating a structure richer in carbon vacancies. The increasing C<sub>b</sub> peak intensity suggests the increase of crystallinity [32]. The C<sub>b</sub> peak intensity of TCN-460 is significantly higher than that of TCN (Fig. 3d), which implies that TCN-460 has fewer internal vacancies due to its ordered crystallinity. The rich vacancies on the surface and ordered crystallinity on the inside of TCN-460 are consistent with PAS and XRD results. The

introduction of carbon vacancies and oxygen doping into the heptazine units is also demonstrated by the  $^{13}\text{C}$  solid-state NMR results (Fig. S2).

As shown in EPR spectra (Fig. 3e), the PCN, TCN, and TCN-460 present one single Lorentzian line with a  $g$  value of 2.0034, which can be attributed to unpaired electrons. Compared with the PCN and TCN samples, TCN-460 has a much higher EPR signal intensity. The higher EPR intensity indicates that a higher concentration of unpaired electrons exists in TCN-460 [33,34]. This is attributed to carbon vacancies and oxygen doping that is introduced into heptazine units and thus creates more unsaturated sites corresponding to unpaired electrons in g-C<sub>3</sub>N<sub>4</sub> [19]; those unpaired electrons can facilitate the production of photoexcited charges. As anticipated, the synergy of carbon vacancies and oxygen doping in TCN-460 enhances the EPR signal compared to PCN and TCN under light irradiation. This result confirms the highly efficient photoexcitation of charges in the TCN-460.

XPS is a highly sensitive characterization method for elemental composition analysis of samples' surfaces and is often used to provide evidence for introducing carbon vacancies and oxygen doping in g-C<sub>3</sub>N<sub>4</sub> [35–37]. As shown in the fitted C 1 s XPS spectra (Fig. 4a), the peak area ratio of terminal C-NH<sub>x</sub> increases gradually with the pyrolytic temperature elevates under water vapor-assisted thermal stripping/etching (Fig. S3a). This shows that the introduction of carbon vacancies leads to more terminal C-NH<sub>x</sub>. The peak area ratio of C-O for TCN and PCN is very small (Fig. S3a), indicating that the melamine precursor and thermal stripping/etching in air do not bring significant oxygen doping into g-C<sub>3</sub>N<sub>4</sub>. The peak area ratio of C-O increases slowly with the increase of pyrolytic temperature. A sharp increase is observed when the temperature exceeds 430 °C (Fig. S3a), indicating that oxygen doping can be introduced into g-C<sub>3</sub>N<sub>4</sub> by the hydrolysis reaction of g-C<sub>3</sub>N<sub>4</sub> with water vapor at high temperatures, and this process mainly occurs after 430 °C.

We also analyzed the fitted O 1 s XPS spectra (Fig. 4b) to demonstrate further the introduction of oxygen doping [38]. Both PCN and TCN show only one peak located at 533.79 eV, attributed to the surface adsorbed adventitious oxygen-containing species (H<sub>2</sub>O, CO<sub>2</sub>, and others). The TCN-400, TCN-430, and TCN-460 exhibit one new peak at 532.09 eV, which is associated with C-O-C. The calculated peak area of C-O-C increases gradually with the rise of pyrolytic temperature under water vapor-assisted thermal stripping/etching. Meanwhile, the oxygen content of TCN-460 (6.58%) obtained from XPS is vastly higher than that of PCN (2.94%). This provides solid evidence that water vapor can act as a source of oxygen to achieve oxygen doping under high-temperature conditions by the hydrolysis reaction with g-C<sub>3</sub>N<sub>4</sub>.

The fitted N 1 s XPS spectra are shown in Fig. 4c. The peak area ratio of N-(C)<sub>3</sub> in TCN-460 is lower than that of TCN (Fig. S3b). This result may be understood in terms of carbon loss originating from the N-(C)<sub>3</sub> sites with its bonds selectively cleaved into N-H<sub>x</sub> fragments [22]. Compared with TCN, the peak area ratio of C-N=C in heptazine rings to the total nitrogen in TCN-460 is significantly lower (Fig. S3b), indicating that oxygen atoms replaced C-N=C bonds on the TCN-460 surface to form C-O-C bonds [38].

The formation energy ( $E_{\text{form}}$ ) calculated by DFT was used to reflect the precise formation position and sequence of carbon vacancies and oxygen doping, as well as the changes in the electronic properties of g-C<sub>3</sub>N<sub>4</sub>. The best position to form carbon vacancies is "1" with  $E_{\text{form}}$  of 0.154 eV, and the best position for introducing oxygen doping is "3" with  $E_{\text{form}}$  of 1.129 eV (Fig. 4e-f). However, the  $E_{\text{form}}$  of oxygen doping is much higher than that of carbon vacancies, so it is easier to introduce carbon vacancies into g-C<sub>3</sub>N<sub>4</sub> at high temperatures. After the carbon vacancies are introduced, the best position of the oxygen doping is "11" with an  $E_{\text{form}}$  of  $-1.34$  eV (Fig. 4h). The negative formation can mean that oxygen doping is more likely to occur dynamically after introducing carbon vacancies. The DFT results are in good agreement with those of XPS; in other words, carbon vacancies are first implanted on g-C<sub>3</sub>N<sub>4</sub>, and then oxygen doping is introduced under water vapor-assisted thermal etching/stripping. The possible formation position and sequence of carbon vacancies and oxygen doping in g-C<sub>3</sub>N<sub>4</sub> are given in Fig. 4j.

The DFT calculated Bader charge is used to reflect the electronic structural properties of g-C<sub>3</sub>N<sub>4</sub>. When carbon vacancies and oxygen doping are introduced, high electron density appears in regions near carbon vacancies (Fig. 4i), while a low electron density characterizes other parts of heptazine units. The charge redistribution leads to strong electron polarization, which minimizes the recombination of photoexcited charges, enhancing the photocatalytic HER activity.

### 3.3. The deep conduction band and the strong reduction ability of TCN-460

It is conceivable that the ultrathin and porous nature of nanosheets with controllable carbon vacancies and oxygen doping can influence the light absorption and optical bandgap of g-C<sub>3</sub>N<sub>4</sub> [39–41]. As UV-vis absorption shows in Fig. 5a, the absorption edge of TCN-460 is blue-shifted compared with PCN and TCN. The bandgap values derived from UV-Vis diffuse reflectance spectra increase with the increase in temperature of water vapor-assisted thermal etching/stripping (Fig. 5b). Valence band X-ray photoelectron spectra (VB-XPS) were employed to determine the electronic structure [42,43]. Fig. 5c manifests  $E_{\text{VB-XPS}}$  first increases with thermal etching/stripping in air and then decreases with the temperature rise of subsequent water vapor-assisted thermal etching/stripping. The formula ( $E_{\text{VB}} = \Phi + E_{\text{VB-XPS}} - 4.44$ ) is used to calculate the VB position ( $E_{\text{VB}}$ ) versus normal hydrogen electrode (NHE) at pH = 7, where  $\Phi$  denotes the electron work function of the analyzer with the value of 3.88 eV [19]. All samples' conduction bands (CB) are calculated by a combined analysis of bandgaps and  $E_{\text{VB-XPS}}$  [44,45]. Fig. 5d reflects that the VB and CB can be continuously regulated by changing the temperature of water vapor-assisted thermal etching/stripping. The increasing CB value implies a stronger reduction potential and a stronger driving force, which is positively correlated with photocatalytic HER.

The density of states (DOS) calculation results by DFT further illustrate the band structure evolution after carbon vacancies and oxygen doping are introduced into g-C<sub>3</sub>N<sub>4</sub>. The DOS calculation and band structure show that the CB occurs due to contributions from C 2p and N 2p orbitals (Fig. 6b). Meanwhile, the composition of CB is mainly ascribed to N 2p orbitals (Fig. 6e). These observations are in agreement with previously reported results [19]. The calculated energy bandgaps are 1.03 eV and 2.74 eV for pure g-C<sub>3</sub>N<sub>4</sub> and g-C<sub>3</sub>N<sub>4</sub> with carbon vacancies and oxygen doping, respectively (Fig. 5c and f). This DFT calculation result indicates that introducing carbon defects and oxygen doping in g-C<sub>3</sub>N<sub>4</sub> can significantly widen the bandgap, which is consistent with UV-Vis diffuse reflectance spectra results.

### 3.4. Efficient photocatalytic H<sub>2</sub> evolution of TCN-460

We evaluated the photocatalytic performance of all samples by investigating photocatalytic HER under visible light irradiation ( $\lambda \geq 420$  nm) and ultraviolet-visible light (780 nm  $\geq \lambda \geq 350$  nm) using triethanolamine (TEOA) as the hole sacrificial agent and 3% platinum (Pt) as the co-catalyst (Fig. S4a-b). Fig. 7a shows that the PCN reference sample has a relatively low HER rate of  $167.4 \mu\text{mol g}^{-1} \text{h}^{-1}$  under visible light irradiation ( $\lambda \geq 420$  nm), while the TCN-460 HER rate drastically increases to  $2414 \mu\text{mol g}^{-1} \text{h}^{-1}$ . TCN-460 HER rate values are 14.42 and 5.91 times that of PCN and TCN, respectively. Considering the increased bandgap and vigorous reduction potential of TCN-460, the photocatalytic HER activity of TCN-460 can reach  $7.414 \text{ mmol g}^{-1} \text{h}^{-1}$  under ultraviolet-visible light (780 nm  $\geq \lambda \geq 350$  nm) excitation, which is 5.2 and 1.9 times that of PCN and TCN, respectively (Fig. 7b). Compared with the typical g-C<sub>3</sub>N<sub>4</sub>, ultrathin g-C<sub>3</sub>N<sub>4</sub> nanosheets fabricated by a similar process, and g-C<sub>3</sub>N<sub>4</sub> with well-tuned band structures, TCN-460 has higher photocatalytic HER activity (Tables S4, S5 and Fig. S12). We highlight the advantages of our step-by-step synergistic etching/stripping strategy by comparing the photocatalytic HER rates of TCN-Ar, PCN-460, and TCN-460 (Fig. 7c). The results show that TCN-

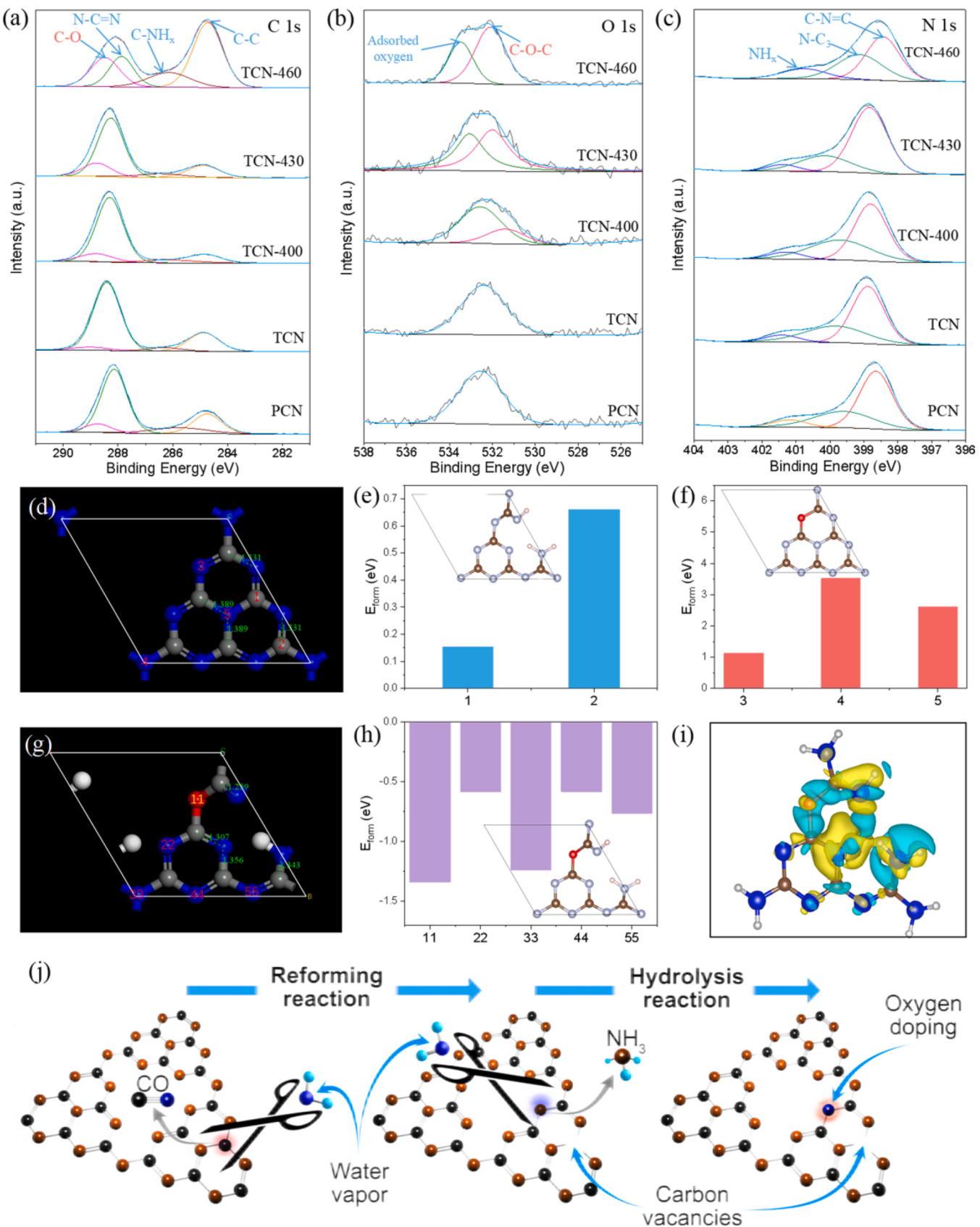


**Fig. 4.** (a) C 1s, (b) O 1s, and (c) N 1s high-resolution XPS spectra of different samples: PCN, TCN, TCN-400, TCN-430, and TCN-460; Model structure in pure g-C<sub>3</sub>N<sub>4</sub> (d) and g-C<sub>3</sub>N<sub>4</sub> with carbon vacancies and oxygen doping sites (g), respectively; The E<sub>form</sub> of (e) carbon vacancies and (f) oxygen doping in pure g-C<sub>3</sub>N<sub>4</sub> and (h) oxygen doping in g-C<sub>3</sub>N<sub>4</sub> with carbon vacancies; (i) Differential charge density distribution of TCN-460 (the yellow and light blue represent electron-rich and electron-deficient regions, respectively); (j) Schematic diagram illustrating the formation of carbon vacancies and oxygen doping g-C<sub>3</sub>N<sub>4</sub>.

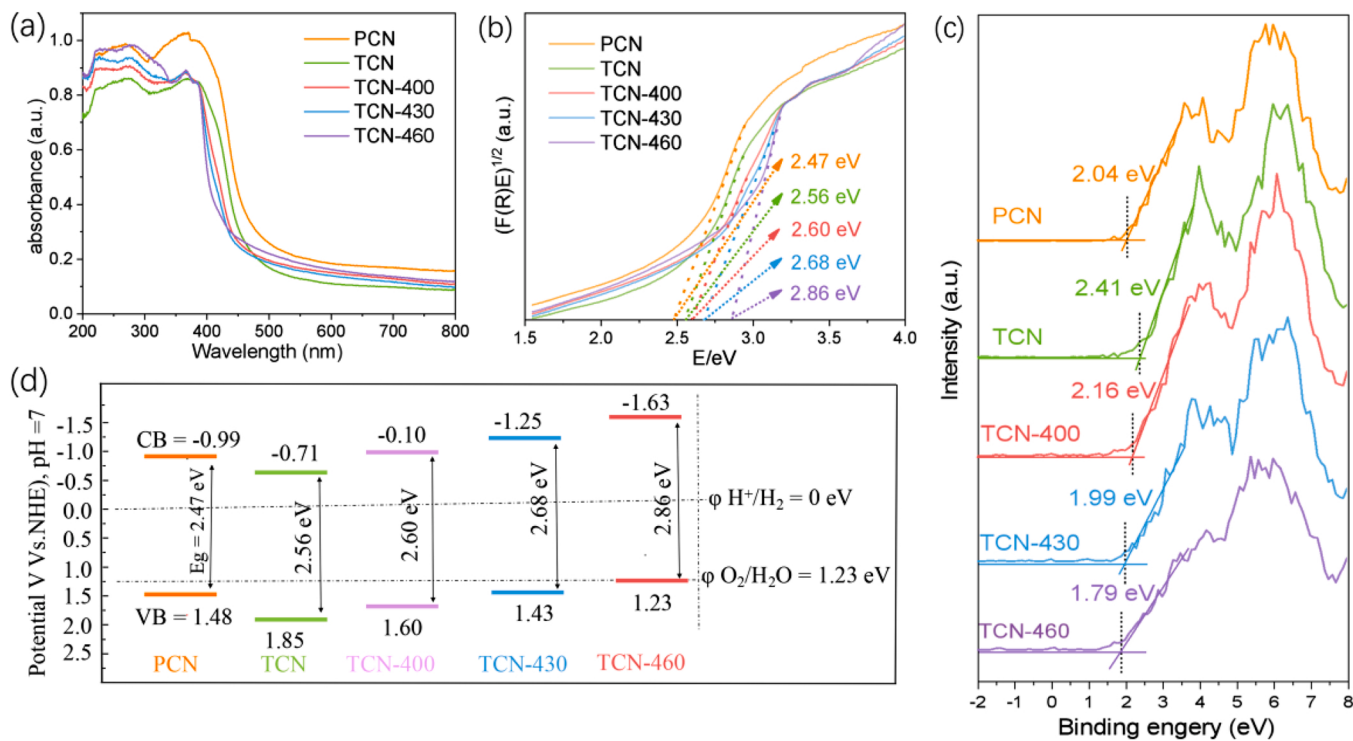


**Fig. 5.** (a) UV-Vis diffuse reflectance spectra, (b) bandgap structure spectra, (c) VB-XPS spectra, and (d) schematic energy band structures of different samples: PCN, TCN, TCN-400, TCN-430, and TCN-460.

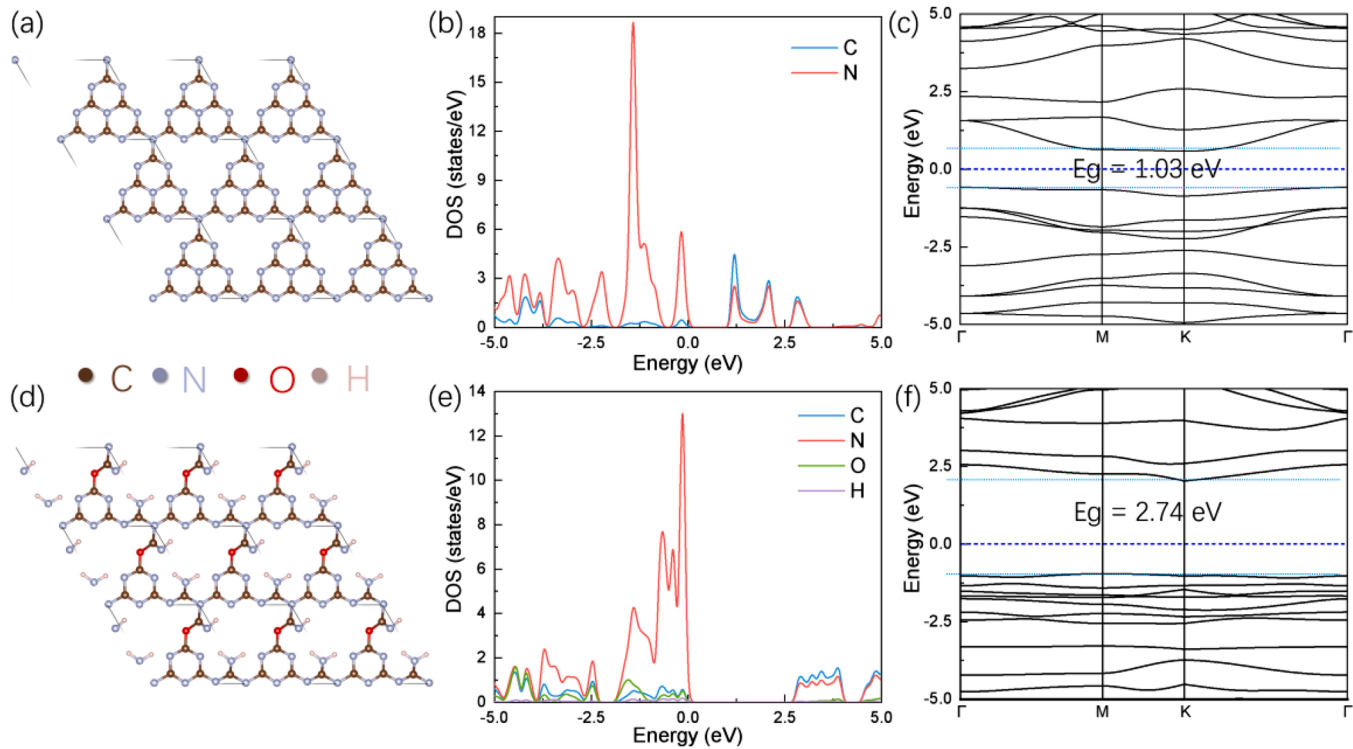


**Fig. 6.** Structure models of pure  $g\text{-C}_3\text{N}_4$  (a) and  $g\text{-C}_3\text{N}_4$  with carbon vacancies and oxygen doping sites (d); Density of states (DOS) and corresponding band structures of pure  $g\text{-C}_3\text{N}_4$  (b, c) and  $g\text{-C}_3\text{N}_4$  with carbon vacancies and oxygen doping sites (e, f).

460 prepared by a step-by-step synergistic etching/stripping strategy exhibits the best photocatalytic performance. Meanwhile, the  $g\text{-C}_3\text{N}_4$  photocatalytic HER activity can be significantly improved by increasing pyrolytic temperature of water vapor-assisted thermal etching/stripping

(Fig. 7d). Commercial  $\text{TiO}_2$  (P25) is the most widely used photocatalyst, but it is limited in the ultraviolet light (UV) region due to its wide bandgap. Therefore, a significant scientific and technological challenge is to develop inexpensive photocatalysts that not only have excellent

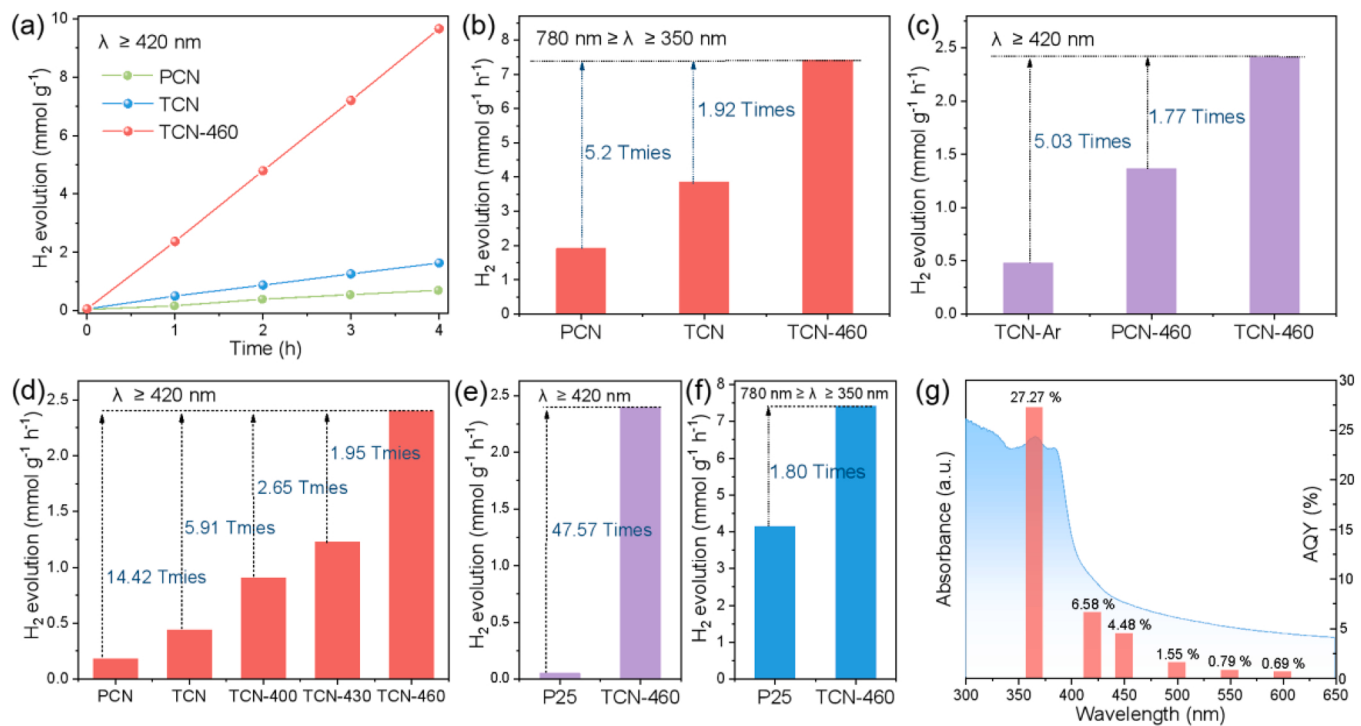


**Fig. 7.** The photocatalytic HER over PCN, TCN, and TCN-460 under (a) visible light ( $\lambda \geq 420$  nm) and (b) ultraviolet-visible light ( $780 \text{ nm} \geq \lambda \geq 350$  nm); (c) The photocatalytic HER over TCN-Ar, PCN-460, and TCN-460; (d) The photocatalytic HER over PCN, TCN, TCN-400, TCN-430, and TCN-460 under visible light ( $\lambda \geq 420$  nm); The photocatalytic HER over P25 and TCN-460 under (e) visible light ( $\lambda \geq 420$  nm) and (f) ultraviolet-visible light ( $780 \text{ nm} \geq \lambda \geq 350$  nm); (g) Apparent quantum yield (AQY) of TCN-460 under different wavelengths of monochromatic light.

photocatalytic HER properties in visible light but also surpass P25 in UV light. TCN-460 shows 47.5 times higher HER than P25 under visible light ( $\lambda \geq 420$  nm) and 1.8 times than P25 under ultraviolet-visible light ( $780 \text{ nm} \geq \lambda \geq 350$  nm) (Fig. 7e, f). These exciting results show that TCN-460 is a better HER photocatalyst than P25 under both visible and UV light. Moreover, TCN-460 can reach AQY values as high as 6.58% and 27.27% at 420 nm and 356 nm monochromatic irradiation, respectively (Fig. 7g and Table S1). UV-vis diffuse reflectance spectra (DRS) results for TCN-460 match the AQY of TCN-460, which further confirms that  $\text{H}_2$  generation was driven by photocatalytic HER. The TCN-460 also demonstrated good stability and high photocatalytic activity at different monochromatic wavelengths, and the detailed description refers to the Supplementary Material (Figs. S5 and S6).

Excited by the impressive HER performance of the TCN-460 system, we further investigated another critical reaction ( $\text{CO}_2$  photoreduction) with strong environmental and industrial values. Compared with PCN and TCN, the TCN-460 photocatalyst achieves the highest  $\text{CO}_2$  photoreduction to  $\text{CH}_4$ , with a yield of  $0.601 \mu\text{mol h}^{-1} \text{ g}^{-1}$  with no cocatalysts or sacrificial agents added, which is 5.83 and 1.62 times of that of PCN and TCN, respectively (Fig. S7).

### 3.5. Photogenerated carriers separation, transfer, and lifetime of TCN-460

After the demonstration of TCN-460 excellent visible light and ultraviolet light-driven photocatalytic performance, it is crucial to reveal the physical mechanism and enhanced factors that determine the photocatalytic processes. Linear sweep voltammetry curves and light response indicate that TCN-460 has a higher anodic current than TCN (Fig. S8). The high current for TCN-460 is attributed to the shorter diffused migration path of photoexcited charges due to its ultrathin, out-of-plane disorder, in-plane ordered structure, and the presence of carbon vacancies and oxygen doping, which further weakens internal electron/hole pairs recombination [46]. The photocurrent response was used to

reflect the separation efficiency of photoexcited charges (Fig. 8a) [47, 48]. The TCN-460 has a higher photocurrent than TCN due to carbon vacancies and the introduction of oxygen doping, making separation of photoexcited charges more efficient under visible light excitation ( $\lambda \geq 420$  nm). Because the TCN-460 has a wider bandgap and stronger reduction potential, the photocurrent signal is enhanced significantly when the excitation light source is ultraviolet-visible light ( $780 \text{ nm} \geq \lambda \geq 350$  nm). This implies that the TCN-460 can give full play to ultraviolet light for photocatalytic HER than TCN. The Nyquist plot of electrochemical impedance spectra in Fig. 8b shows that TCN-460 possesses a smaller semicircle than TCN in the dark [49]. The impedance of TCN-460 is significantly smaller than TCN under illumination due to the significantly reduced migration resistance for photoexcited charges in TCN-460. The surface photovoltage spectroscopy (SPS) was used to reveal further photoexcited charges' separation and transfer behavior under illumination (Fig. S10). TCN-460 has a stronger surface photovoltage signal than TCN, which indicates that TCN-460 has a faster separation of photoexcited charges, supporting outstanding photocatalytic activity. These observations indicate that TCN-460 has a faster charge migration and separation rate than TCN. To further study the transfer property of photoexcited charges, both the steady-state PL and time-resolved PL decay spectra were recorded and analyzed [50, 51]. The PL emission intensity of TCN-460 is much lower than of TCN and PCN (Fig. 8c) due to a suppressed recombination of photoexcited charges. The peak location indicates a significant blue shift which is attributed to the ultrathin structure due to the quantum confinement effect [52]. However, compared with PCN, the fluorescence intensity of TCN does not decrease, and the corresponding position of the emission peak is blue-shifted. This phenomenon can be ascribed to the decrease in conjugation length and the strong quantum confinement effect due to the single-layer structure of  $\text{g-C}_3\text{N}_4$  nanosheets [52–54]. Furthermore, this observation reflects that the stacked nanosheets in PCN undergoing thermal etching/stripping in air were successfully stripped into small-layer nanosheets. The PL lifetime of TCN-460 is shorter compared

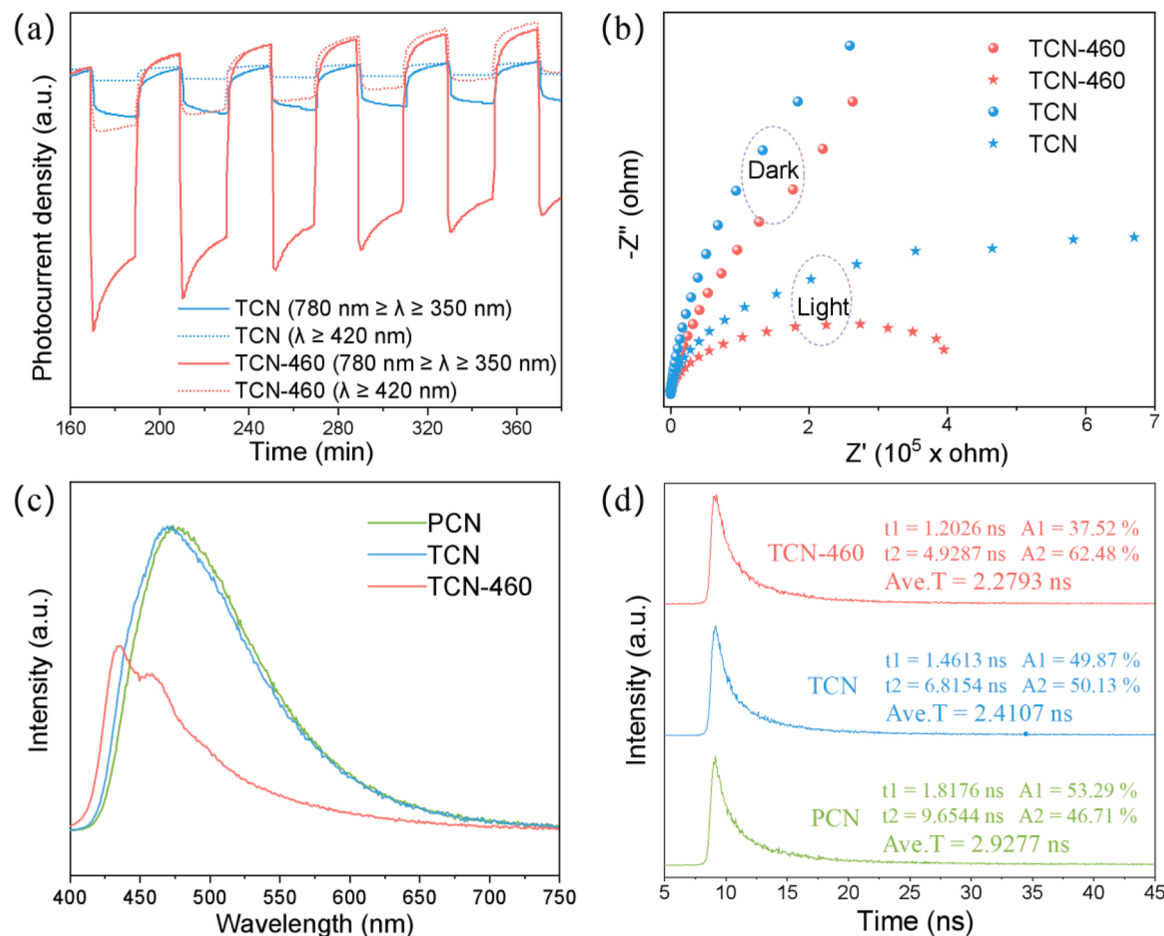


**Fig. 8.** (a) Switching photocurrent spectra of TCN and TCN-460 under visible light ( $\lambda \geq 420$  nm) and ultraviolet-visible light ( $780 \text{ nm} \geq \lambda \geq 350$  nm), respectively; (b) Switching Nyquist plot of electrochemical impedance spectra of TCN and TCN-460 under visible light ( $\lambda \geq 420$  nm); (c) The steady-state PL spectra and (d) time-resolved PL decay spectra (excitation wavelength 380 nm) of PCN, TCN, and TCN-460.

with PCN and TCN (Fig. 8d). The short PL lifetime suggests that carbon vacancies and oxygen doping as charge trapping centers can efficiently capture photoexcited charges, resulting in improved separation and transfer efficiency [21].

### 3.6. The enhancement factors and mechanism for photocatalytic HER

DFT calculations were used to explore the promoting effect of Pt modification on  $\text{H}^+$  activation and  $\text{H}_2$  production on photocatalysts (see the structural model in Fig. S11a) [55]. The whole  $\text{H}_2$  production process is usually composed of the initial state ( $\text{H}^+ + \text{e}^-$ ), intermediate state (adsorbed  $\text{H}^*$ ), and product ( $1/2 \text{ H}_2$ ). The  $\Delta G_{\text{H}^*}$  of the intermediate state obtained by DFT is considered the main indicator in the whole  $\text{H}_2$  production process. The closer  $\Delta G_{\text{H}^*}$  is to zero, the more conducive it is to photocatalytic  $\text{H}_2$  production. As shown in Fig. S11b, the Pt-loaded  $\text{g-C}_3\text{N}_4$  has significantly negative  $\Delta G_{\text{H}^*}$  ( $-1.14$  eV), which means strong adsorption of intermediate  $\text{H}^*$ , which is not conducive to photocatalytic  $\text{H}_2$  production. The  $\Delta G_{\text{H}^*}$  of Pt-loaded TCN-460 is  $-0.086$  eV, which is closer to zero than Pt-loaded  $\text{g-C}_3\text{N}_4$ . This means that Pt-loaded TCN-460 has the mediated adsorption-desorption property and the promoted  $\text{H}^+$  activation. Therefore, Pt-loaded TCN-460 is more beneficial to the  $\text{H}_2$  production reaction. The electronic localization function obtained by calculation reflects the change of electronic structure caused by Pt-loaded TCN-460. As shown in Fig. S11c and d, more electrons will be extracted from TCN-460 and transferred to the surface of Pt, resulting in an efficient  $\text{H}_2$  production reaction on the surface of Pt.

It is widely acknowledged that the four main factors that determine high-efficiency photocatalysis are 1) interface contact, 2) light absorption, 3) generation, separation, and migration of photoexcited charges, and 4) drivable reduction-oxidation of surface catalysis. Each step is closely related to the photocatalyst's morphology, defects, doping, and band structure. The 2D ultrathin nanosheets of TCN-460 with high porosity and large specific surface area as well as out-of-plane disorder and in-plane ordered structure provide easily accessible channels for the interface contact between reactant molecules and catalysts and significantly shorten the perpendicular migration distance of photoexcited charges, accelerating electrons transport along the in-plane direction. Secondly, the synergy of carbon vacancies and oxygen doping provides charge trapping centers to efficiently capture photoexcited charges, resulting in a significantly enhanced charge separation and transfer. In addition, the charges redistribution caused by carbon vacancies and oxygen doping gained by DFT calculation would lead to strong electron polarization to minimize the recombination of photogenerated charges (Fig. 4i). Last but not least, the vigorous reduction potential of TCN-460 with a wide bandgap provides a powerful driving force for photocatalytic water splitting, resulting in an excellent photocatalytic hydrogen evolution.

Based on these analyses and discussions above, the photocatalytic enhancement mechanism is proposed in Scheme S1. TCN-460 absorbs photons to excite electrons from the VB to the CB, while the holes are set in the VB [56]. Afterward, the electron transfer from TCN-460 to Pt cocatalyst promotes the aggregation of electrons on the Pt surface with adequate  $\Delta G_{\text{H}^*}$ , which is beneficial to photocatalytic  $\text{H}_2$  production.

Thus, effective reduction-oxidation occurs in the water/triethanolamine (TEOA) system, further resulting in an effective photocatalytic H<sub>2</sub> production.

In summary, this work features several novelty points: 1) The first time that high-temperature water vapor is used to introduce controllable carbon vacancies and oxygen doping into g-C<sub>3</sub>N<sub>4</sub> and achieve efficient stripping into ultrathin nanosheets. 2) We showed the continuous regulation of g-C<sub>3</sub>N<sub>4</sub>'s band structure readily achieved by introducing controllable carbon vacancies and oxygen doping. 3) An outstanding photocatalytic performance of our samples surpassing other ultrathin g-C<sub>3</sub>N<sub>4</sub> nanosheets prepared by similar processes and other g-C<sub>3</sub>N<sub>4</sub> with well-tuned band structure (see comparisons in Tables S5 and S6).

#### 4. Conclusion

To sum up, ultrathin and porous g-C<sub>3</sub>N<sub>4</sub> nanosheets were successfully fabricated with controllable carbon vacancies and oxygen doping via a facile and green step-by-step synergistic etching/stripping strategy. Our method does not require any harmful or expensive chemicals but only water vapor, which introduces controllable carbon vacancies on g-C<sub>3</sub>N<sub>4</sub> and subsequently serves as an oxygen source to realize steerable oxygen doping of g-C<sub>3</sub>N<sub>4</sub> at high temperatures. The synergistic effect of controllable carbon vacancies and oxygen doping in ultrathin and porous g-C<sub>3</sub>N<sub>4</sub> nanosheets significantly enhances photo-excited charges' separation and migration by suppressing recombination. Furthermore, due to the adjustable electronic structure of g-C<sub>3</sub>N<sub>4</sub> nanosheets by changing the temperature of water vapor-assisted thermal etching/stripping, the higher reduction potential of TCN-460 provides a strong driving force for photocatalytic HER. As expected, the synthesized TCN-460 shows excellent photocatalytic HER rates as high as 2.414 mmol g<sup>-1</sup> h<sup>-1</sup> under visible light irradiation ( $\lambda \geq 420$  nm), over one order of magnitude higher than pristine g-C<sub>3</sub>N<sub>4</sub>. Moreover, TCN-460 also exhibits 7.414 mmol g<sup>-1</sup> h<sup>-1</sup> photocatalytic HER activity under ultraviolet-visible light (780 nm  $\geq \lambda \geq 350$  nm), which is 5.2 times higher than pristine g-C<sub>3</sub>N<sub>4</sub>. This work not only provides a facile and green step-by-step synergistic etching/stripping strategy to controllably construct carbon vacancies and oxygen doping on the surface of g-C<sub>3</sub>N<sub>4</sub> but also provides thought-provoking insights on developing clean and effective methods for stripping other 2D materials (e.g., MXenes) for advanced photocatalytic applications.

#### CRediT authorship contribution statement

**Bin Yang:** Investigation, Formal analysis, Methodology, Conceptualization, Visualization, Writing – original draft, Writing – review & editing. **Xiaolong Li:** Investigation, Formal analysis, Methodology, Visualization. **Qian Zhang:** Investigation, Visualization, Writing – review & editing. **Xiaodong Yang:** Investigation, Methodology, Visualization. **Jianguo Wan:** Investigation, Methodology, Visualization. **Guangfu Liao:** Resources, Visualization, Funding acquisition, Writing – review & editing. **Jiaojiao Zhao:** Investigation, Methodology, Visualization. **Rongjie Wang:** Investigation, Methodology, Visualization. **Jichang Liu:** Investigation, Methodology, Visualization. **Raul D. Rodriguez:** Resources, Writing – draft and editing, Visualization, Funding acquisition, Writing - review & editing. **Xin Jia:** Resources, Writing – draft and editing, Visualization, Funding acquisition.

#### Declaration of Competing Interest

The authors declare that they have no known competing financial interests or personal relationships that could have appeared to influence the work reported in this paper.

#### Acknowledgments

This research was supported by the National Natural Science

Foundation of China (U1703351, 52073179, 51663021), the Programme of Introducing Talents of Discipline to Universities (D20018), Overseas Professor Project in Bingtuan, Bingtuan Excellent Young Scholars (CZ027205), Bingtuan Science & Technology Nova, and Startup Funding for Scientific Research of China University of Geosciences (Wuhan). RDR also acknowledges the TPU Priority 2030 development program.

#### Appendix A. Supplementary material

Supplementary data associated with this article can be found in the online version at doi:10.1016/j.apcatb.2022.121521.

#### References

- [1] G. Liao, C. Li, S.-Y. Liu, B. Fang, H. Yang, Emerging frontiers of Z-scheme photocatalytic systems, *Trends Chem.* 4 (2022) 111–127.
- [2] J. Chen, K. Li, X. Li, X. Fan, J. Chen, K. Lv, Preparation and modification of crystalline carbon nitride, *Chin. J. Inorg. Chem.* 37 (2021) 1713–1726.
- [3] G. Liao, Y. Gong, L. Zhang, H. Gao, G. Yang, B. Fang, Semiconductor polymeric graphitic carbon nitride photocatalysts: the "holy grail" for the photocatalytic hydrogen evolution reaction under visible light, *Energy Environ. Sci.* 12 (2019) 2080–2147.
- [4] G. Liao, C. Li, X. Li, B. Fang, Emerging polymeric carbon nitride Z-scheme systems for photocatalysis, *Cell Rep. Phys. Sci.* 2 (2021), 100355.
- [5] D. Zhao, Y. Wang, C. Dong, Y. Huang, J. Chen, F. Xue, S. Shen, L. Guo, Boron-doped nitrogen-deficient carbon nitride-based Z-scheme heterostructures for photocatalytic overall water splitting, *Nat. Energy* 6 (2021) 388–397.
- [6] L. Luo, Z. Gong, J. Ma, K. Wang, H. Zhu, K. Li, L. Xiong, X. Guo, J. Tang, Ultrathin sulfur-doped holey carbon nitride nanosheets with superior photocatalytic hydrogen production from water, *Appl. Catal. B Environ.* 284 (2021), 119742.
- [7] Y. Li, M. Gu, X. Zhang, J. Fan, K. Lv, S.A.C. Carabineiro, F. Dong, 2D g-C<sub>3</sub>N<sub>4</sub> for advancement of photo-generated carrier dynamics: status and challenges, *Mater. Today* 41 (2020) 270–303.
- [8] C. Dong, Z. Ma, R. Qie, X. Guo, C. Li, R. Wang, Y. Shi, B. Dai, X. Jia, Morphology and defects regulation of carbon nitride by hydrochloric acid to boost visible light absorption and photocatalytic activity, *Appl. Catal. B Environ.* 217 (2017) 629–636.
- [9] M. Zhu, S. Kim, L. Mao, M. Fujitsuka, J. Zhang, X. Wang, T. Majima, Metal-free photocatalyst for H<sub>2</sub> evolution in visible to near-infrared region: black phosphorus/graphitic carbon nitride, *J. Am. Chem. Soc.* 139 (2017) 13234–13242.
- [10] Y. Li, X. Xu, J. Wang, W. Luo, Z. Zhang, X. Cheng, J. Wu, Y. Yang, G. Chen, S. Sun, L. Wang, Post-redox engineering electron configurations of atomic thick C<sub>3</sub>N<sub>4</sub> nanosheets for enhanced photocatalytic hydrogen evolution, *Appl. Catal. B Environ.* 207 (2020), 118855.
- [11] K. Li, M. Zhang, X. Ou, R. Li, Q. Li, J. Fan, K. Lv, Strategies for the fabrication of 2D carbon nitride nanosheets, *Acta Phys. Chim. Sin.* 37 (2021), 2008010.
- [12] X. Dong, F. Cheng, Recent development in exfoliated two-dimensional g-C<sub>3</sub>N<sub>4</sub> nanosheets for photocatalytic applications, *J. Mater. Chem. A* 3 (2015) 23642–23652.
- [13] N. Meng, J. Ren, Y. Liu, Y. Huang, T. Petit, B. Zhang, Engineering oxygen-containing and amino groups into two-dimensional atomically-thin porous polymeric carbon nitrogen for enhanced photocatalytic hydrogen production, *Energy Environ. Sci.* 11 (2018) 566–571.
- [14] Z. Sun, W. Wang, Q. Chen, Y. Pu, H. He, W. Zhuang, J. He, L. Huang, A hierarchical carbon nitride tube with oxygen doping and carbon defects promotes solar-to-hydrogen conversion, *J. Mater. Chem. A* 8 (2020) 3160–3167.
- [15] Z. Huang, J. Song, L. Pan, Z. Wang, X. Zhang, J. Zou, W. Mi, X. Zhang, L. Wang, Carbon nitride with simultaneous porous network and O-doping for efficient solar-energy-driven hydrogen evolution, *Nano Energy* 12 (2015) 646–656.
- [16] L. Yang, J. Huang, L. Shi, L. Cao, Q. Yu, Y. Jie, J. Fei, H. Ouyang, J. Ye, A surface modification resultant thermally oxidized porous g-C<sub>3</sub>N<sub>4</sub> with enhanced photocatalytic hydrogen production, *Appl. Catal. B Environ.* 204 (2017) 335–345.
- [17] A. Kumar, P. Raizada, A. Hosseini-Bandegharaei, V. Thakur, V. Nguyen, P. Singh, C, N-Vacancy defect engineered polymeric carbon nitride towards photocatalysis: viewpoints and challenges, *J. Mater. Chem. A* 9 (2021) 111–153.
- [18] S. Li, G. Dong, R. Hailili, L. Yang, Y. Li, Y. Fu Wang, C. Zeng, Wang, Effective photocatalytic H<sub>2</sub>O<sub>2</sub> production under visible light irradiation at g-C<sub>3</sub>N<sub>4</sub> modulated by carbon vacancies, *Appl. Catal. B Environ.* 190 (2016) 26–35.
- [19] D. Zhao, C. Dong, W. Bin, C. Chen, Y. Huang, Z. Diao, S. Li, L. Guo, S. Shen, Synergy of dopants and defects in graphitic carbon nitride with exceptionally modulated band structures for efficient photocatalytic oxygen evolution, *Adv. Mater.* 31 (2019), 1903545.
- [20] G. Liu, Y. Huang, H. Lv, H. Wang, Y. Zeng, M. Yuan, Q. Meng, C. Wang, Confining single-atom Pd on g-C<sub>3</sub>N<sub>4</sub> with carbon vacancies towards enhanced photocatalytic NO conversion, *Appl. Catal. B Environ.* 284 (2021), 119683.
- [21] P. Yang, L. Shang, J. Zhao, M. Zhang, H. Shi, H. Zhang, H. Yang, Selectively constructing nitrogen vacancy in carbon nitrides for efficient syngas production with visible light, *Appl. Catal. B Environ.* 297 (2021), 120496.
- [22] P. Yang, H. Ou, Y. Fang, X. Wang, A facile steam reforming strategy to delaminate layered carbon nitride semiconductors for photoredox catalysis, *Angew. Chem. Int. Ed.* 56 (2017) 3992–3996.

[23] P. Yang, H. Zhuzhang, R. Wang, W. Lin, X. Wang, Carbon vacancies in a melon polymeric matrix promote photocatalytic carbon dioxide conversion, *Angew. Chem. Int. Ed.* 58 (2019) 1134–1143.

[24] Y. Zhang, G. Li, J. Wang, D. Luo, Z. Sun, Y. Zhao, A. Yu, X. Wang, Z. Chen, “Sauna” activation toward intrinsic lattice deficiency in carbon nanotube microspheres for high-energy and long-lasting lithium-sulfur batteries, *Adv. Energy Mater.* 11 (2021), 2100497.

[25] B.C. Ranu, D.C. Sarkar, A simple, efficient, and highly selective method for the regeneration of carbonyl compounds from oximes and semicarbazones, *J. Org. Chem.* 53 (1988) 878–879.

[26] P. Niu, L. Zhang, G. Liu, H. Cheng, Graphene-like carbon nitride nanosheets for improved photocatalytic activities, *Adv. Funct. Mater.* 22 (2012) 4763–4770.

[27] X. Wu, X. Wang, F. Wang, H. Yu, Soluble g-C<sub>3</sub>N<sub>4</sub> nanosheets: facile synthesis and application in photocatalytic hydrogen evolution, *Appl. Catal. B Environ.* 247 (2019) 70–77.

[28] X. Li, Z. Hu, Q. Li, M. Lei, J. Fan, S.A.C. Carabineiro, Y. Liu, K. Lv, Three in one: atomically dispersed Na boosting the photoreactivity of carbon nitride towards NO oxidation, *Chem. Commun.* 56 (2020) 14195–14198.

[29] Y. Kang, Y. Yang, L. Yin, X. Kang, G. Liu, H. Cheng, An amorphous carbon nitride photocatalyst with greatly extended visible-light-responsive range for photocatalytic hydrogen generation, *Adv. Mater.* 27 (2015) 4572–4577.

[30] S. Wang, H. Zhao, X. Zhao, J. Zhang, Z. Ao, P. Dong, F. He, H. Wu, X. Xu, L. Shi, C. Zhao, S. Wang, H. Sun, Surface engineering of hollow carbon nitride microspheres for efficient photoredox catalysis, *Chem. Eng. J.* 381 (2020), 122593.

[31] X. Wang, J. Meng, X. Zhang, Y. Liu, M. Ren, Y. Yang, Y. Guo, Controllable approach to carbon-deficient and oxygen-doped graphitic carbon nitride: robust photocatalyst against recalcitrant organic pollutants and the mechanism insight, *Adv. Funct. Mater.* 31 (2021), 2010763.

[32] D. Zhao, J. Chen, C. Dong, W. Zhou, Y. Huang, S.S. Mao, L. Guo, S. Shen, Interlayer interaction in ultrathin nanosheets of graphitic carbon nitride for efficient photocatalytic hydrogen evolution, *J. Catal.* 352 (2017) 491–497.

[33] G. Dong, D.L. Jacobs, L. Zang, C. Wang, Carbon vacancy regulated photoreduction of NO to N<sub>2</sub> over ultrathin g-C<sub>3</sub>N<sub>4</sub> nanosheets, *Appl. Catal. B Environ.* 218 (2017) 515–524.

[34] Y. Liang, X. Wu, X. Liu, C. Li, S. Liu, Recovering solar fuels from photocatalytic CO<sub>2</sub> reduction over W<sup>6+</sup>-incorporated crystalline g-C<sub>3</sub>N<sub>4</sub> nanorods by synergistic modulation of active centers, *Appl. Catal. B Environ.* 304 (2022), 120978.

[35] C. Li, X. Liu, G. Ding, P. Huo, Y. Yan, Y. Yan, G. Liao, Interior and surface synergistic modifications modulate the SnNb<sub>2</sub>O<sub>6</sub>/Ni-doped ZnIn<sub>2</sub>S<sub>4</sub> S-scheme heterojunction for efficient photocatalytic H<sub>2</sub> evolution, *Inorg. Chem.* 61 (2022) 4681–4689.

[36] G. Zhang, Y. Xu, C. He, P. Zhang, H. Mi, Oxygen-doped crystalline carbon nitride with greatly extended visible-light-responsive range for photocatalytic H<sub>2</sub> generation, *Appl. Catal. B Environ.* 283 (2021), 119636.

[37] C. Li, G. Ding, X. Liu, P. Huo, Y. Yan, Y. Yan, G. Liao, Photocatalysis over NH<sub>2</sub>-UiO-66/CoFe<sub>2</sub>O<sub>4</sub>/CdIn<sub>2</sub>S<sub>4</sub> double p-n junction: significantly promoting photocatalytic performance by double internal electric fields, *Chem. Eng. J.* 435 (2022), 134740.

[38] Y. Chen, X. Liu, L. Hou, X. Guo, R. Fu, J. Sun, Construction of covalent bonding oxygen-doped carbon nitride/graphitic carbon nitride Z-scheme heterojunction for enhanced visible-light-driven H<sub>2</sub> evolution, *Chem. Eng. J.* 383 (2020), 123132.

[39] Y. Zhu, C. Lv, Z. Yin, J. Ren, X. Yang, C. Dong, H. Liu, R. Cai, Y. Huang, W. Theis, S. Shen, D. Yang, 001-Oriented Hittorf's phosphorus nanorods/polymeric carbon nitride heterostructure for boosting wide-spectrum-responsive photocatalytic hydrogen evolution from pure water, *Angew. Chem. Int. Ed.* 59 (2020) 868–873.

[40] Y. Zhang, Z. Huang, C. Dong, J. Shi, C. Cheng, X. Guan, S. Zong, B. Luo, Z. Cheng, D. Wei, Y. Huang, S. Shen, L. Guo, Synergistic effect of nitrogen vacancy on ultrathin graphitic carbon nitride porous nanosheets for highly efficient photocatalytic H<sub>2</sub> evolution, *Chem. Eng. J.* 431 (2022), 134101.

[41] J. Ma, D. Jin, Y. Li, D. Xiao, G. Jiao, Q. Liu, Y. Guo, L. Xiao, X. Chen, X. Li, J. Zhou, R. Sun, Photocatalytic conversion of biomass-based monosaccharides to lactic acid by ultrathin porous oxygen doped carbon nitride, *Appl. Catal. B Environ.* 283 (2021), 119520.

[42] L. Wang, Y. Hong, E. Liu, X. Duan, X. Lin, J. Shi, A bottom-up acidification strategy engineered ultrathin g-C<sub>3</sub>N<sub>4</sub> nanosheets towards boosting photocatalytic hydrogen evolution, *Carbon* 163 (2020) 234–243.

[43] M. Wang, Y. Zeng, G. Dong, C. Wang, Br-doping of g-C<sub>3</sub>N<sub>4</sub> towards enhanced photocatalytic performance in Cr(VI) reduction, *Chin. J. Catal.* 41 (2020) 1498–1510.

[44] Y. Hong, C. Li, Z. Fang, B. Luo, W. Shi, Rational synthesis of ultrathin graphitic carbon nitride nanosheets for efficient photocatalytic hydrogen evolution, *Carbon* 121 (2017) 463–471.

[45] Q. Liu, C. Chen, K. Yuan, C. Sewell, Z. Zhang, X. Fang, Z. Lin, Robust route to highly porous graphitic carbon nitride microtubes with preferred adsorption ability via rational design of one-dimension supramolecular precursors for efficient photocatalytic CO<sub>2</sub> conversion, *Nano Energy* 77 (2020), 105104.

[46] C. Han, P. Su, B. Tan, X. Ma, H. Lv, C. Huang, P. Wang, Z. Tong, G. Li, Y. Huang, Z. Liu, Defective ultrathin two-dimensional g-C<sub>3</sub>N<sub>4</sub> photocatalyst for enhanced photocatalytic H<sub>2</sub> evolution activity, *J. Colloid Interface Sci.* 581 (2021) 159–166.

[47] D. Qin, Y. Xia, Q. Li, C. Yang, Y. Qin, K. Lv, One-pot calcination synthesis of Cd<sub>0.5</sub>Zn<sub>0.5</sub>S/g-C<sub>3</sub>N<sub>4</sub> photocatalyst with a step-scheme heterojunction structure, *J. Mater. Sci. Technol.* 56 (2020) 206–215.

[48] C. Yang, Q. Tan, Q. Li, J. Zhou, J. Fan, B. Li, J. Sun, K. Lv, 2D/2D Ti<sub>3</sub>C<sub>2</sub> MXene/g-C<sub>3</sub>N<sub>4</sub> nanosheets heterojunction for high efficient CO<sub>2</sub> reduction photocatalyst: dual effects of urea, *Appl. Catal. B Environ.* 268 (2020), 118738.

[49] B. Yang, J. Zheng, W. Li, R. Wang, D. Li, X. Guo, R.D. Rodriguez, X. Jia, Engineering Z-scheme TiO<sub>2</sub>-OV-BiOCl via oxygen vacancy for enhanced photocatalytic degradation of imidacloprid, *Dalton Trans.* 49 (2020) 11010–11018.

[50] M. Wu, Y. Gong, T. Nie, J. Zhang, R. Wang, H. Wang, B. He, Template-free synthesis of nanocage-like g-C<sub>3</sub>N<sub>4</sub> with high surface area and nitrogen defects for enhanced photocatalytic H<sub>2</sub> activity, *J. Mater. Chem. A* 7 (2019) 5324–5332.

[51] Q. Liu, H. Cheng, T. Chen, T. Lo, Z. Xiang, F. Wang, Regulating the \*OCCHO intermediate pathway towards highly selective photocatalytic CO<sub>2</sub> reduction to CH<sub>3</sub>CHO over locally crystallized carbon nitride, *Energy Environ. Sci.* 15 (2022) 225–233.

[52] B. Yang, Z. Wang, J. Zhao, X. Sun, R. Wang, G. Liao, X. Jia, 1D/2D carbon-doped nanowire/ultra-thin nanosheet g-C<sub>3</sub>N<sub>4</sub> isotype heterojunction for effective and durable photocatalytic H<sub>2</sub> evolution, *Int. J. Hydrog. Energy* 46 (2021) 25436–25447.

[53] J. Xu, L. Zhang, R. Shi, Y. Zhu, Chemical exfoliation of graphitic carbon nitride for efficient heterogeneous photocatalysis, *J. Mater. Chem. A* 1 (2013) 14766–14772.

[54] J. Yi, T. Fei, L. Li, Q. Yu, S. Zhang, Y. Song, J. Lian, X. Zhu, J. Deng, H. Xu, H. Li, Large-scale production of ultrathin carbon nitride-based photocatalysts for high-yield hydrogen evolution, *Appl. Catal. B Environ.* 281 (2021), 119475.

[55] L. Jiang, J. Li, K. Wang, G. Zhang, Y. Li, X. Wu, Low boiling point solvent mediated strategy to synthesize functionalized monolayer carbon nitride for superior photocatalytic hydrogen evolution, *Appl. Catal. B Environ.* 260 (2020), 118181.

[56] J. Wu, N. Li, H. Fang, X. Li, Y. Zheng, X. Tao, Nitrogen vacancies modified graphitic carbon nitride: scalable and one-step fabrication with efficient visible-light-driven hydrogen evolution, *Chem. Eng. J.* 358 (2019) 20–29.